Icarus 291 (2017) 75–81

Contents lists available at ScienceDirect

Icarus

journal homepage: www.elsevier.com/locate/icarus

Subsurface structures of buried features in the lunar Procellarum region

Wenrui Wang[a,b,*], Kosuke Heki[b]

[a] National Astronomical Observatories, Chinese Academy of Sciences, Beijing, China
[b] Department of Earth and Planetary Sciences, Hokkaido University, Sapporo, Japan

ARTICLE INFO

Article history:
Received 25 November 2016
Revised 19 March 2017
Accepted 22 March 2017
Available online 23 March 2017

Keyword:
Procellarum
Buried features
Substructure
GRAIL
Inversion

ABSTRACT

The Gravity Recovery and Interior Laboratory (GRAIL) mission unraveled numbers of features showing strong gravity anomalies without prominent topographic signatures in the lunar Procellarum region. These features, located in different geologic units, are considered to have complex subsurface structures reflecting different evolution processes. By using the GRAIL level-1 data, we estimated the free-air and Bouguer gravity anomalies in several selected regions including such intriguing features. With the three-dimensional inversion technique, we recovered subsurface density structures in these regions.

1. Introduction

The lunar Procellarum region encompasses Oceanus Procellarum, Mare Imbrium, and the adjoining maria and highlands. It is characterized by low elevation, thin crust, and high concentrations of heat-producing elements (Andrews-Hanna et al., 2014), and especially by extended volcanic activities (Grimm, 2013). It has been postulated that a sub-crustal thick radionuclide layer caused complex thermal condition during the lunar evolution, and influenced the morphology and internal structures of this region (Wieczorek and Phillips, 2000). Past studies focused mainly on morphology and mineralogy (Campbell et al., 2009; Head and Gifford, 1980; Lawrence et al., 2013; McEwen et al., 1994; Mustard et al., 2011; Wöhler et al., 2006), and lack detailed studies of interior structures and their evolution.

Analyses of topography-gravity admittance using coefficients derived in spherical harmonic expansions have been effective in studying lunar interior structures, but this approach is only applicable in global domain (Wieczorek, 2007; Wieczorek et al., 2013). Although localization techniques can adjust this method to local and regional studies (Huang et al., 2014; Kiefer, 2004, 2013; Wieczorek and Simons, 2005, 2007), they introduce intrinsic spectral leakage (Wieczorek and Simons, 2005) and the Gibbs phenomenon.

In comparison with these studies, satellite orbit perturbations are considered to reflect gravity anomaly more directly, and the inversion of substructure from such perturbation signals is a straightforward approach. As orbit perturbation decays with the distance, this approach is suitable for local studies and has high calculation efficiency. Sugano and Heki (2004) applied this method to resolve lunar gravity anomalies with the Lunar Prospector line-of-sight (LOS) data. With the low-low satellite-to-satellite tracking (SST) technique, Gravity Recovery and Interior Laboratory (GRAIL) measures inter-satellite range-rates and accelerations that are sensitive to gravity signatures of small-scale features. In this paper, we use the level-1 data from the GRAIL mission to study buried features in several selected area within the Procellarum region.

2. Methodology

2.1. Data sources and regions of interest

Launched in 2011 as one of the lunar exploration missions, GRAIL has been contributing to discoveries of new features on the Moon in terms of gravity anomalies. The primary science phase lasted from 7 Mar. 2012 to 29 May 2012, followed by the second science phase from 30 Aug. to 14 Dec. 2012 (Zuber et al., 2016). The GRAIL data are categorized in 3 levels. The level-1 data are the expanded, edited and calibrated data (Asmar et al., 2013). GRAIL level-1 files are comprised of inter-satellite K-band range-rate data, satellite coordinates, attitudes and accelerometer data. The twin-satellite system lets common errors acting on both satellites cancel each other and amplify short-wavelength gravity signals (Kim and Tapley, 2002). From the Planetary Data System

* Corresponding author.
E-mail address: wangwr@nao.cas.cn (W. Wang).

http://dx.doi.org/10.1016/j.icarus.2017.03.025
0019-1035/

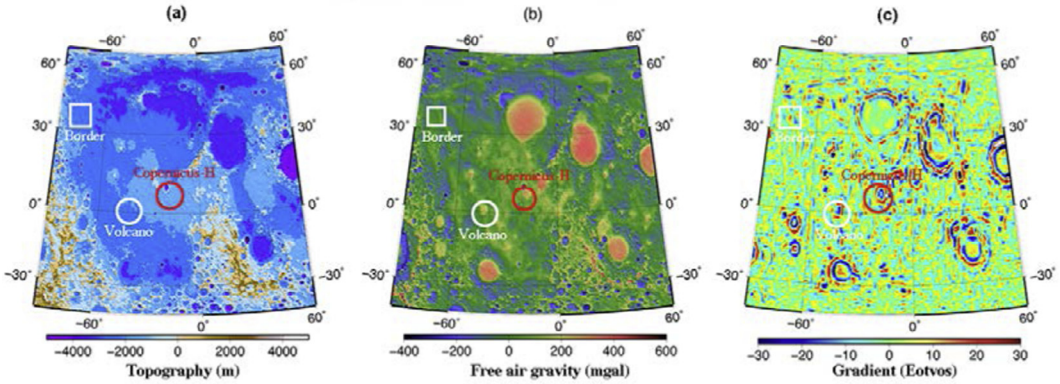

Fig. 1. Regions of interests marked on topography map (a), free-air gravity map (b) and Bouguer gravity gradient map (c). The topography map is derived from the LRO (Lunar Reconnaissance Orbiter) topography model lro_ltm05_2050_sha (truncated at 600), and the GRAIL gravity model jggrx_1500e_sha (truncated at 600). The gradient map is derived from maximum horizontal gradient method. The red circle is newly defined buried crater Copernicus-H (Neumann et al., 2015), and white circle shows the buried feature near volcanic complexes. White square represents the hexagon border. (For interpretation of the references to color in this figure legend, the reader is referred to the web version of this article.)

Table 1
Center coordinates of ROIs.

ROI name	Longitude	Latitude
Copernicus-H	−18° E	7° N
Volcano	−45° E	0° N
Border	−75° E	35° N

(PDS), we download the observation data over two months period (September–October, 2012) covering the whole Procellarum region.

We combine the topography and gravity maps (Fig. 1) to study regions of interests (ROIs), especially the buried features (i.e. without topography manifestation) with prominent gravity anomalies. Compared with the topography map (Fig. 1a), the free air gravity map (Fig. 1b) show anomalous features more clearly, making mascons and the hexagon border conspicuous. Besides, gravitational potential gradients (Eq. (1)) help us highlight the circular and linear structures (Andrews-Hanna et al., 2013).

$$\Gamma_{hh} = \begin{vmatrix} \Gamma_{11} & if\ \Gamma_{11} > abs(\Gamma_{22}) \\ \Gamma_{22} & if\ \Gamma_{11} < abs(\Gamma_{22}) \end{vmatrix}, \quad (1)$$

where Γ_{hh} is the maximum horizontal gradient, Γ_{11} and Γ_{22} are horizontal gradient tensor representing the value of the maximum and minimum curvature of the Bouguer gravity anomaly.

We select three ROIs in different geologic units. They are simply flat in the topography map (Fig. 1a), but have positive anomalies in the gravity anomaly map (Fig. 1b). In the gravity gradient map (Fig. 1c), these ROIs display explicit features. The first ROI (red circle) is close to mascons and defined as Copernicus-H (Neumann et al., 2015), while the second ROI (white circle) lies near volcanoes and belongs to one of the volcanic complexes named Flamsteed (Yamamoto et al., 2016). The third ROI lies on the hexagon border (the white square) enclosing the Procellarum region. Each region covers a 10°×10° (10° corresponds to ~300 km on the lunar surface) area with the center coordinates listed in Table 1.

2.2. Gravity inversion from level-1 data

Gravity inversion from the level-1 data is based on point-mass method (Sugano and Heki, 2004). There we assumed that the excess masses responsible for the gravity anomalies are condensed on a thin layer on the lunar reference surface, and the gravitational forces by these excess masses are calculated through the Newton's theory. We divided each ROI (10° × 10° in size) into a set of small blocks. ROI is the unit of least-squares estimation runs, and the small blocks included in ROI correspond to the parameters (point masses at the centers of the blocks) to be estimated. The point mass separation (or spatial resolution) is set to 0.3°×0.3° (~9 km × 9 km), sufficient to resolve short-wavelength mass anomalies.

We used a software system similar to those used in Sugano and Heki (2004), after changing the input data from the Lunar Prospector LOS acceleration data to the GRAIL KBRR (K-band range rate) data. The observation equations at satellite position i are shown in (Eq. (2)), indicating the orbit perturbations caused by the mass anomaly of a small block.

$$\begin{cases} \delta_i = \vec{a}_{ai} - \vec{a}_{bi} \\ \vec{a}_{ai} = G\sum_{j=1}^{M} \frac{m_j}{r_{aij}^3} \cdot \vec{s}_{ai} \\ \vec{a}_{bi} = G\sum_{j=1}^{M} \frac{m_j}{r_{bij}^3} \cdot \vec{s}_{bi} \end{cases}, \quad (2)$$

where δ_i is the difference between $\vec{a}_{ai}$ and $\vec{a}_{bi}$, accelerations of the two satellites caused by a small mass block. M is the total number of small blocks, G is the universal gravitational constant, m_j is the mass anomaly of the jth block, r_{aij} is the distance between the jth block and the satellite a (r_{bij} the distance between the block and the satellite b), $\vec{s}_{ai}$ and $\vec{s}_{bi}$ are projection vectors to the inter-satellite baseline $\overline{ab}$.

Bouguer gravity anomaly is derived from the terrain corrected free-air gravity anomaly, so it is more sensitive to the subsurface mass inhomogeneity and suitable for the subsequent substructure inversion. We used the 0.25° gridded topography model from Lunar Reconnaissance Orbiter (LRO) for the terrain correction, and generated the Bouguer gravity anomaly map. To avoid singularity in the following steps, Bouguer anomalies are upward continued to 10 km height above the 1738 km lunar reference sphere.

2.3. Subsurface density inversion

Because subsurface density distributions vary not only laterally but also vertically, the three dimensional (3-D) inversion is necessary to recover variations. The lunar radius is much less than the Earth, so we need to consider its curvature for larger depths. Here 3we implement 3-D inversion in a spherical domain, known as tesseroid method. Each research region is divided into a set of contiguous spherical tesseroids (Anderson, 1976) with a constant density. The gravitational potential and gravity of tesseroid are

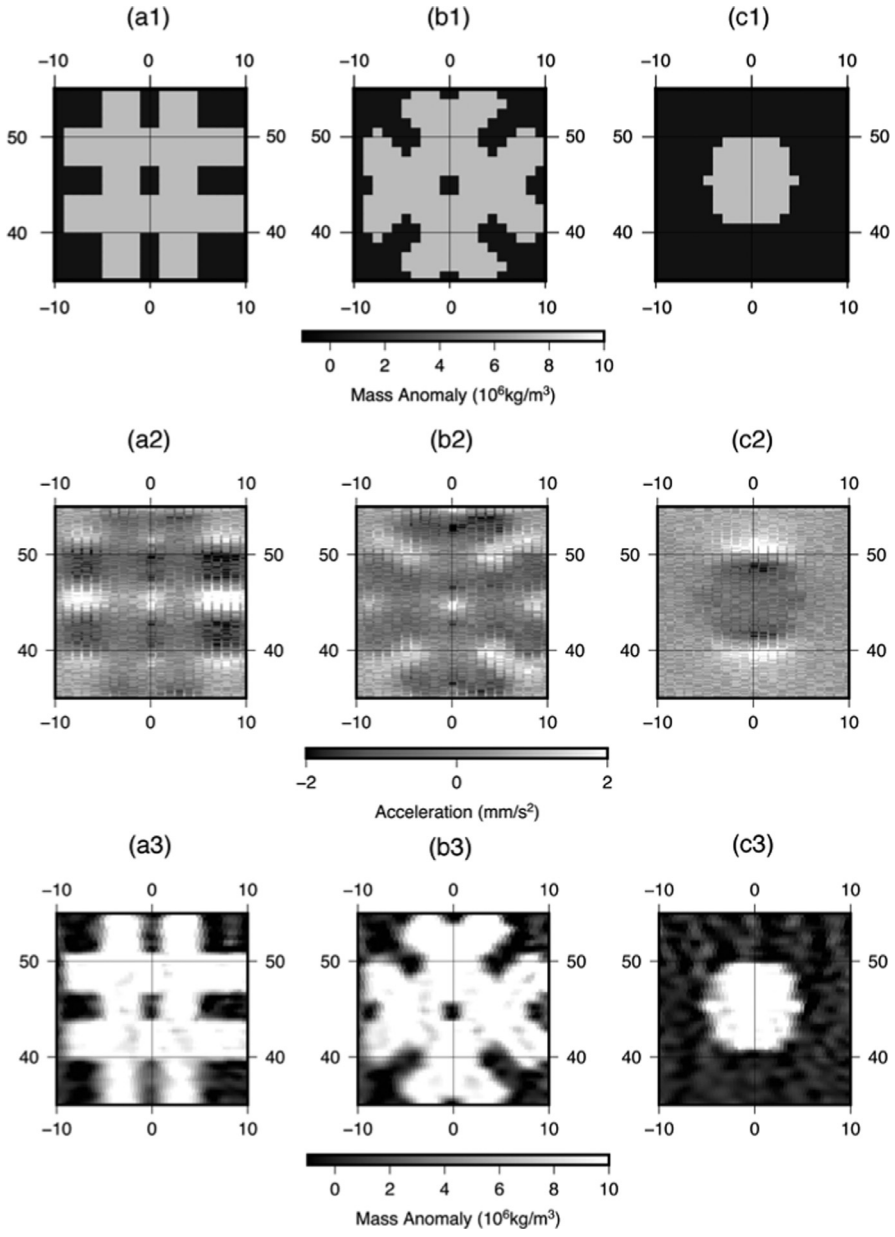

Fig. 2. Original models (a1, b1, c1), synthetic accelerations data with random noises (a2, b2, c2), and inversion results (a3, b3, c3). The centers are set at (45°N, 0°E). Noises appear close to the edge of the large block, and the vague boundaries of the recovered structures are partly caused by the continuity constraints imposed in the inversion.

described by Newton's integral as in (Eq. (3)).

$$V(r,\phi,\lambda) = G\rho \int_{\lambda_1}^{\lambda_2}\int_{\phi_1}^{\phi_2}\int_{r_1}^{r_2} \frac{1}{l} k dr' d\phi' d\lambda'$$

$$g_\alpha(r,\phi,\lambda) = G\rho \int_{\lambda_1}^{\lambda_2}\int_{\phi_1}^{\phi_2}\int_{r_1}^{r_2} \frac{\Delta_\alpha}{l^3} k dr' d\phi' d\lambda' \quad \alpha \in x,y,z \tag{3}$$

where G is the universal gravitational constant, l denotes the Euclidean distance between the computation point $P(r, \phi, \lambda)$ and the running integration point $Q(r', \phi', \lambda')$, and ψ is the angle between the position vectors of the two points.

$$\Delta_x = r' K_\phi$$

$$\Delta_y = r' cos\phi' \sin(\lambda' - \lambda)$$

$$\Delta_z = r' cos\psi - r$$

$$l = \sqrt{r^2 + r'^2 - 2rr' cos\psi}$$

$$cos\psi = sin\phi sin\phi' + cos\phi cos\phi' \cos(\lambda' - \lambda)$$

$$K_\phi = cos\phi sin\phi' - sin\phi cos\phi' \cos(\lambda' - \lambda)$$

$$k = r'^2 cos\phi' \tag{4}$$

After discretization and linearization, tesseroid gravity function is transformed into the following form.

$$\delta g_i = \sum_j^M \rho_j A_{ij}, \quad i = 1, \ldots, N \tag{5}$$

where δg_i is the observation data, ρ_j is the tesseroid density, and A_{ij} is element of the kernel matrix (Liang et al., 2014).

In order to solve this ill-posed problem, we applied the Tikhonov regularization to the normal matrix (Tikhonov and Arsenin, 1977), and used the L-curve criterion to find the optimal regularization parameter (Hansen, 1992). The latest lunar crustal thickness model (Wieczorek et al., 2013) was used to determine the maximum inversion depth. Each least-squares run was performed over a region as large as 10° × 10° × 60 km (~300 km

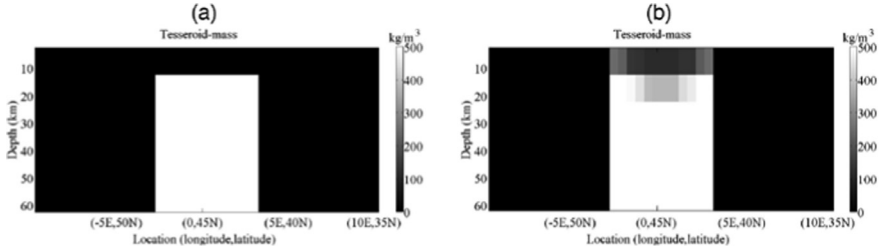

Fig. 3. Tesseroid model profile (a) and recovered structure profile (b).

× 300 km × 60 km), which include blocks, corresponding to parameters to be estimated, as large as 0.5° × 0.5° × 5 km (~15 km × 15 km × 5 km).

2.4. Validation of method

Before applying the inversion software to real data, we validated the method to confirm its accuracy and sensitivity. We design three synthetic models to test the point-mass inversion method. Two sets of ridges composed of lunar crustal rock (600 km long, 90 km wide, and 3 km high) are put in the middle latitude parallel to lunar latitude/longitude lines (Fig. 2a1) and with the angle of 45° to them (Fig. 2b1) to test the azimuth dependence of the sensitivity to surface linear features. For a more realistic test for our research objects, sensitivity to a disk simulating a lunar crater is also examined (Fig. 2c1).

Considering that the published level-1b data may contain non-calibrated accelerations due to solar radiation forces, sloshing fuel and vibration from the momentum wheels, here we added random noises into the inter-satellite accelerations to test their influences on the inversion results (Fig. 2a2–c2). We added the random noises of ~1 mm/s^2, which is ~3 times as large as the scatter of the original accelerations over the studied region.

Recovered structures from point-mass inversion are shown in Fig. 2a3–c3. We use correlation coefficients between original models and inversion results to test recovered results. The correlation coefficients are 0.928, 0.960 and 0.922 without noises, and 0.923, 0.960 and 0.922 after the noises were added. So the additional random noises do not contribute much to the inversion results. As continuity constraint is added to stabilize the solution in the least-squares calculation to suppress abrupt changes between adjacent blocks, the outlines of the recovered textures have been blurred to some extent. However, recovered structures show high similarity to features with different azimuths. We also confirmed that this is the case for regions of different latitudes or longitudes. The disk was also well-recovered, and this demonstrates the validity of our method in this research.

To test the three-dimensional inversion method, a simple model is constructed and was tried to recover. In this model, a block shaped structure (5° × 5° × 50 km) is buried at 10–60 km depth under the lunar surface, with a density contrast of 500 kg/m^3(Fig. 3 a). The synthetic inversion results are shown in Fig. 3b. Although some noises appear near the top boundary of the recovered sheet at depth, the recovery result reproduces the overall shape and density contrast of the original structure.

3. Results and discussion

3.1. Free-air and Bouguer gravity anomalies

Recovered free-air and Bouguer gravity anomalies are displayed in Fig. 4. Red color represents excess mass while blue color represents mass deficit. By subtracting components due to topography

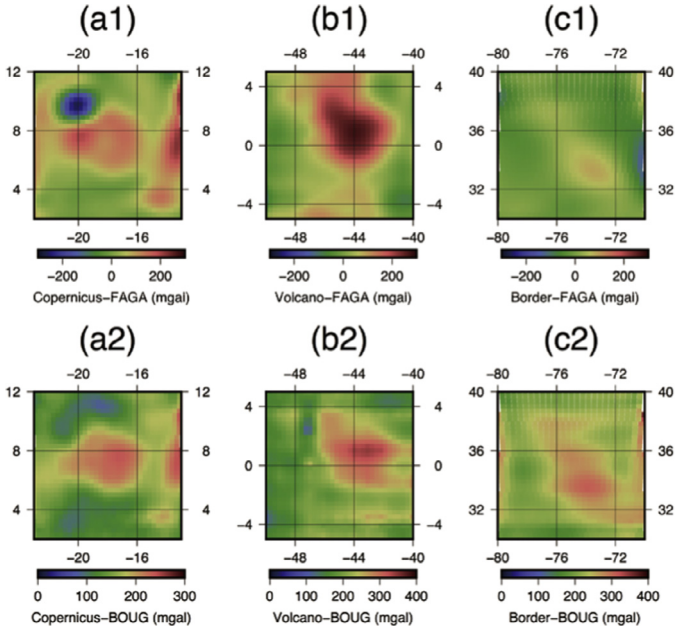

Fig. 4. Recovered free-air gravity anomalies (FAGA) (a1, b1, c1) and Bouguer gravity anomalies (BOUG) (a2, b2, c2) in the three ROIs.

from the raw data and estimating mass anomalies, we get the Bouguer gravity anomalies that highlight the subsurface features.

Copernicus-H displays regular circular gravity anomaly with central high values and annular low surrounding features. The central peak values are considered to come from uplifted mantle material, while the annuli corresponds to rings of thickened sub-isostatic crust originating from the ejecta (Wieczorek and Phillips, 1999). Volcano region displays elongated-shaped gravity anomalies which are postulated to arise from frequent volcanic activities (Haskin et al., 2000). Complex structures such as magma chamber, sill, intrusive sheet, or cumulate prisms probably exist underneath, just like other shield volcanoes nearby (e.g. Marius, Aristarchus, and Kepler). The hexagon border possesses linear positive gravity anomalies running NW-SE, with negative anomalies on both sides. It represents the dike structure formed by large-scale crustal rifting and magma uplift.

3.2. Three-dimensional density structures

Bouguer gravity anomalies reflect density contrasts at depth, and we reconstructed the vertical and radial density distributions here. Based on the crustal thickness model by (Wieczorek et al., 2013) derived from the Lunar Prospector, Kaguya and GRAIL data, the maximum crustal thickness of 60 km is used as the depth limit of the density structure inversion.

Vertical profiles along the white lines in Fig. 5 are given in Fig. 6 to show the recovered structures more clearly. Density

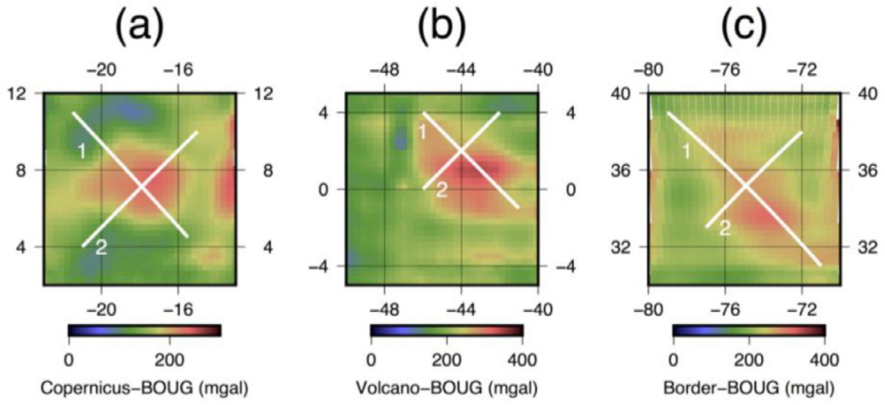

Fig. 5. White lines showing the surface trace of the vertical profiles in Fig. 6. They run through Copernicus-H (a), volcano (b) and hexagon border (c). Profile 1 runs from northwest to southeast (NW-SE) and profile 2 runs from southwest to northeast (NE-SW).

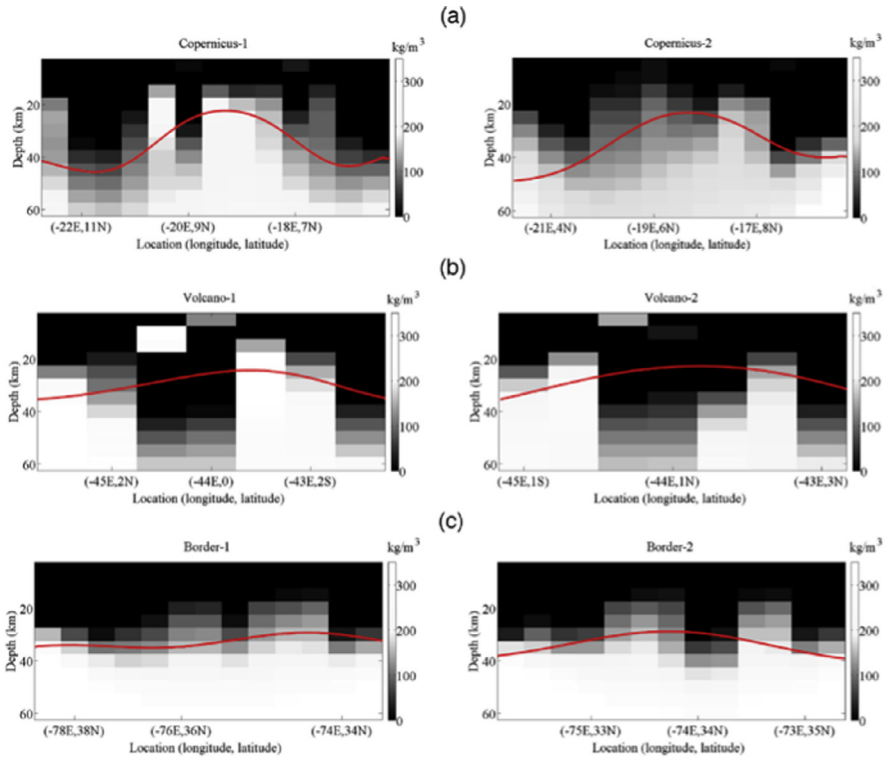

Fig. 6. Density contrast profiles of (a) Copernicus-H, (b) volcano region and (c) border region, in which profile 1 runs from northwest to southeast (NW-SE) and profile 2 runs from northeast to southwest (NE-SW). Density contrasts are defined relative to the average crustal density of 2550 kg/m^3. We also draw red curves indicating the mantle-crust boundary curves, derived from the crust model by Wieczorek et al. (2013). (For interpretation of the references to color in this figure legend, the reader is referred to the web version of this article.)

contrasts are relative to the mean crustal density of 2550 kg/m^3 (Wieczorek et al., 2013). Existing density models show the crustal density within 2660–2820 kg/m^3 (Besserer et al., 2014) and the mantle density with 3000–4000 kg/m^3(Matsuyama et al., 2016), so we made the density contrast color bars to cover the range 0–350 kg/m^3, sharpening the crust-mantle boundary.

In comparison, we pick the same ROI profiles from the GRAIL crust model (Wieczorek et al., 2013) and show them in . The crust-mantle boundary undulations share similarity to the recovered density structures, fluctuating in the depths range 20–40 km (our results recover more details in the subsurface structures). The density inversion errors in the boundaries (as shown in Fig. 3) may have obscured the abrupt change of density to some extent.

Crater Copernicus at the northwest corner of Copernicus-H region is a fresh complex crater, with flat crater floor and sheet-like layers in the steep crater wall. It is well preserved and less degraded after impact. The ejecta blanket compositions are investigated within ~1 crater radii beyond the rims of this impact crater (Ishiyama et al., 2013; Weider et al., 2010), and the ejecta can also be recognized from topography map as brown circular region in Fig. 7a. Except ejecta blanket, both the crater bottom and the outer area are covered with evenly distributed high-density lava flow. Here we apply a method similar to the Bouguer correction to estimate average mare density and verify the 3D inversion results.

A lattice inside the crater floor and two lattices outside the crater are selected as the checkpoints. The outer ones are separately located 2-radii and 3-radii distances away from the crater center, to avoid the ejecta blanket effect. The separation between the lattice points is set to 0.3°, and the topography and gravity at each point are compared in Fig. 7b.

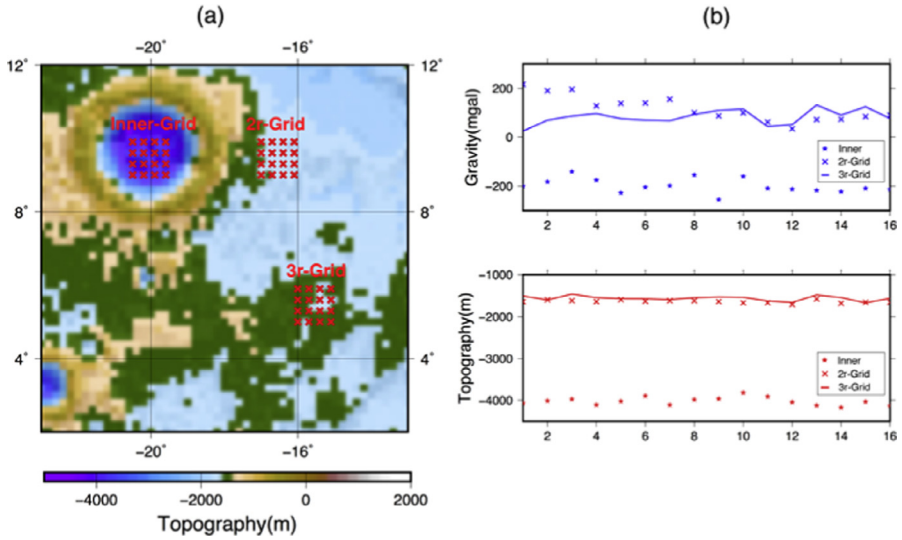

Fig. 7. Lattices inside and outside the crater Copernicus (a), and the topographic height and gravity at 16 points within the lattice (b). The two outer lattices are located about 2-radii and 3-radii away from the center of the crater Copernicus, marked as red crosses. (For interpretation of the references to color in this figure legend, the reader is referred to the web version of this article.)

Table 2
Statistics of topography and gravity of checkpoints.

Lattices	Maximum		Minimum		Mean	
	Topography (m)	Gravity (mgal)	Topography (m)	Gravity (mgal)	Topography (m)	Gravity (mgal)
Inner-Grid	−3820	−141	−4174	−255	−4023.5	−198.9
2r-Grid	−1578	216	−1711	34	−1639.9	117.0
3r-Grid	−1464	132	−1670	24	−1564.2	83.3

The topography and gravity curves of all three lattices are relatively stable, indicating flat topography and homogeneous material in this region. The prominent separation between the inner and the outer lattices is mainly caused by height difference. We treat the outer area as a "Bouguer plate" relative to the crater bottom.

The topography and gravity statistics are listed in Table 2, and we do the following calculation using their mean values. With the Bouguer correction formula $\delta g = 2\pi G\rho\delta h$, where $\delta g = g_{outer} - g_{inner}$ and $\delta h = h_{outer} - h_{inner}$, we derive the mare density as 2950 kg/m^3.

Reading from the topography map, the depth of the flat-bottomed crater Copernicus is about 4 km, corresponding to the first layer (0–5 km) of the inverted 3-D density matrix. The average value of the matrix is 2925 kg/m^3, very close to 2950 kg/m^3 derived above. This also substantiate the inversion results.

3.3. Discussion

Substructures of the three buried features demonstrate their various origins and evolution processes. We hypothesize that the subsurface structures in the Copernicus-H region were formed mainly by impact cratering. On the other hand, those beneath the other two research ROIs would have originated from volcanic activities. To study their formation sequences, we review chronological researches. Researchers such as Heisinger and Morota and their groups mapped the ages of mare basalts using the crater size-frequency diagram (CSFD) (Hiesinger et al., 2003; Hiesinger et al., 2000; Morota et al., 2011). From these studies, the hexagon border region is assumed to be ~3.5 Ga, and the volcano region is probably ~1.5 Ga. The age of the Copernicus-H region is unclear, but the Clementine UVVIS spectral image shows that this region is covered by dark blue and purple minerals. Zhang et al. (2014) developed an empirical model to correlate the Clementine images to spectral types and geologic ages of basalt. According to this model, we can estimate the age of the Copernicus-H region to be 3.25–2.25 Ga, older than the hexagon border but younger than the volcano region.

We propose the following hypotheses based on thermodynamics of the Procellarum region. Lithosphere was heated by the KREEP layer for billions of years, and during its cooling period, tensional cracks and rift zones emerged, and this was followed by magma intrusions (Andrews-Hanna et al., 2013; 2014). Hexagon border is the earliest generated large-scale magma intrusion, and it was followed by the impact cratering incidents that formed Copernicus-H. Excess lithospheric stress around impact craters encouraged the developments of more cracks and rifts, and subsequent intrusion from magma chamber formed younger volcanoes.

4. Conclusions

The GRAIL level-1 data are comprised of inter-satellite range rate and acceleration that are sensitive to subsurface mass anomalies, and enable us to recover high-resolution subsurface density structures. We picked up the level-1data taken above three areas of flat topography in the Procellarum region with possible interesting buried substructures, i.e. the Copernicus-H region, the volcano region, and the hexagon border region. With the point mass method, we estimated free-air and Bouguer gravity anomalies in the regions including these three features. The recovered gravity anomalies suggested that uplifted mantle may exist beneath Copernicus-H, and that complex volcanic intrusions exist under the volcano region and the hexagon border region. We further investigated detailed 3-D density structures. The density profiles of the studied regions showed variety of subsurface boundaries with density contrasts, and suggested their different evolution mechanisms. Combined with geologic ages, we conclude that hexagon border was the oldest, generated from thermal contraction about 3.5 billion years ago. Copernicus-H was caused as an impact cratering about 3.25–2.25 billion years ago, and the volcano region is the youngest, probably formed by the magma intrusion into the cracks and rifts whose formation was encouraged by nearby impact craters.

Acknowledgments

This work is funded by the National Natural Science Foundation of China (Grant No. 41304021, No. 11503055) and CAS-sponsored Overseas Scholarship Program. The authors appreciate H. J. Melosh and an anonymous reviewer for constructive comments, and Dr. Zhang Yi for discussions on density inversion processing work. This paper owes partly to the 2015 Master thesis of Mina Hashimoto, Hokkaido University.

References

Anderson, E.G., 1976. The Effect of Topography on Solutions of Stokes' Problem. School of Surveying, University of New South Wales, Kensington, NSW, Australia.

Andrews-Hanna, J.C., Asmar, S.W., Head, J.W., Kiefer, W.S., Konopliv, A.S., Lemoine, F.G., Matsuyama, I., Mazarico, E., McGovern, P.J., Melosh, H.J., 2013. Ancient igneous intrusions and early expansion of the Moon revealed by GRAIL gravity gradiometry. Science 339, 675–678.

Andrews-Hanna, J.C., Besserer, J., Head, J.W.,3rd, Howett, C.J., Kiefer, W.S., Lucey, P.J., McGovern, P.J., Melosh, H.J., Neumann, G.A., Phillips, R.J., Schenk, P.M., Smith, D.E., Solomon, S.C., Zuber, M.T., 2014. Structure and evolution of the lunar Procellarum region as revealed by GRAIL gravity data. Nature 514, 68–71.

Asmar, S.W., Konopliv, A.S., Watkins, M.M., Williams, J.G., Park, R.S., Kruizinga, G., Paik, M., Yuan, D.-N., Fahnestock, E., Strekalov, D., 2013. The scientific measurement system of the gravity recovery and interior laboratory (GRAIL) mission. Space Sci. Rev. 178, 25–55.

Besserer, J., Nimmo, F., Wieczorek, M.A., Weber, R.C., Kiefer, W.S., McGovern, P.J., Andrews-Hanna, J.C., Smith, D.E., Zuber, M.T., 2014. GRAIL gravity constraints on the vertical and lateral density structure of the lunar crust. Geophys. Res. Lett. 41, 5771–5777.

Campbell, B.A., Hawke, B.R., Campbell, D.B., 2009. Surface morphology of domes in the Marius hills and Mons Rümker regions of the Moon from Earth-based radar data. J. Geophys. Res.: Planets 114.

Grimm, R.E., 2013. Geophysical constraints on the lunar Procellarum KREEP Terrane. J. Geophys. Res.: Planets 118, 768–778.

Hansen, P.C., 1992. Analysis of discrete ill-posed problems by means of the L-curve. SIAM Rev. 34, 561–580.

Haskin, L.A., Gillis, J.J., Korotev, R.L., Jolliff, B.L., 2000. The materials of the lunar Procellarum KREEP Terrane: a synthesis of data from geomorphological mapping, remote sensing, and sample analyses. J. Geophys. Res.-All Series 105 (20), 403–420 416.

Head, J.W., Gifford, A., 1980. Lunar mare domes: classification and modes of origin. Moon Planets 22, 235–258.

Hiesinger, H., Head, J.W., Wolf, U., Jaumann, R., Neukum, G., 2003. Ages and stratigraphy of mare basalts in oceanus procellarum, mare nubium, mare cognitum, and mare insularum. J. Geophys. Res.: Planets 108.

Hiesinger, H., Jaumann, R., Neukum, G., Head, J.W., 2000. Ages of mare basalts on the lunar nearside. J. Geophys. Res.: Planets 105, 29239–29275.

Huang, Q., Xiao, Z., Xiao, L., 2014. Subsurface structures of large volcanic complexes on the nearside of the Moon: a view from GRAIL gravity. Icarus 243, 48–57.

Ishiyama, K., Kumamoto, A., Ono, T., Yamaguchi, Y., Haruyama, J., Ohtake, M., Katoh, Y., Terada, N., Oshigami, S., 2013. Estimation of the permittivity and porosity of the lunar uppermost basalt layer based on observations of impact craters by SELENE. J. Geophys. Res.: Planets 118, 1453–1467.

Kiefer, W.S., 2004. Gravity evidence for an extinct magma chamber beneath Syrtis Major, Mars: a look at the magmatic plumbing system. Earth Planet Sc. Lett. 222, 349–361.

Kiefer, W.S., 2013. Gravity constraints on the subsurface structure of the Marius hills: the magmatic plumbing of the largest lunar volcanic dome complex. J. Geophys. Res.: Planets 118, 733–745.

Kim, J., Tapley, B.D., 2002. Error analysis of a low-low satellite-to-satellite tracking mission. J. Guidance Control Dyn. 25, 1100–1106.

Lawrence, S.J., Stopar, J.D., Hawke, B., Greenhagen, B.T., Cahill, J.T.S., Bandfield, J.L., Jolliff, B.L., Denevi, B.W., Robinson, M.S., Glotch, T.D., 2013. LRO observations of morphology and surface roughness of volcanic cones and lobate lava flows in the Marius hills. J. Geophys. Res.: Planets 118, 615–634.

Liang, Q., Chen, C., Li, Y., 2014. 3-D inversion of gravity data in spherical coordinates with application to the GRAIL data. J. Geophys. Res.: Planets 119, 1359–1373.

Matsuyama, I., Nimmo, F., Keane, J.T., Chan, N.H., Taylor, G.J., Wieczorek, M.A., Kiefer, W.S., Williams, J.G., 2016. GRAIL, LLR, and LOLA constraints on the interior structure of the Moon. Geophys. Res. Lett. 43, 8365–8375.

McEwen, A.S., Robinson, M.S., Eliason, E.M., Lucey, P.G., 1994. Clementine observations of the Aristarchus region of the Moon. Science 266, 1858.

Morota, T., Haruyama, J., Ohtake, M., Matsunaga, T., Honda, C., Yokota, Y., Kimura, J., Ogawa, Y., Hirata, N., Demura, H., 2011. Timing and characteristics of the latest mare eruption on the Moon. Earth Planet Sc. Lett. 302, 255–266.

Mustard, J.F., Pieters, C.M., Isaacson, P.J., Head, J.W., Besse, S., Clark, R.N., Klima, R.L., Petro, N.E., Staid, M.I., Sunshine, J.M., 2011. Compositional diversity and geologic insights of the Aristarchus crater from Moon mineralogy mapper data. J. Geophys. Res.: Planets 116.

Neumann, G.A., Zuber, M.T., Wieczorek, M.A., Head, J.W., Baker, D.M., Solomon, S.C., Smith, D.E., Lemoine, F.G., Mazarico, E., Sabaka, T.J., Goossens, S.J., Melosh, H.J., Phillips, R.J., Asmar, S.W., Konopliv, A.S., Williams, J.G., Sori, M.M., Soderblom, J.M., Miljkovic, K., Andrews-Hanna, J.C., Nimmo, F., Kiefer, W.S., 2015. Lunar impact basins revealed by gravity recovery and interior laboratory measurements. Sci Adv 1, e1500852.

Sugano, T., Heki, K., 2004. High resolution lunar gravity anomaly map from the lunar prospector line-of-sight acceleration data. Earth Planet. Space 56, 81–86.

Tikhonov, A.N., Arsenin, V.Y., 1977. Solutions of Ill-Posed Problems. Halsted Press, New York.

Weider, S.Z., Crawford, I.A., Joy, K.H., 2010. Individual lava flow thicknesses in Oceanus Procellarum and Mare Serenitatis determined from Clementine multispectral data. Icarus 209, 323–336.

Wieczorek, M.A., 2007. The gravity and topography of the terrestrial planets. Treatise Geophys 2007 10, 165–206.

Wieczorek, M.A., Neumann, G.A., Nimmo, F., Kiefer, W.S., Taylor, G.J., Melosh, H.J., Phillips, R.J., Solomon, S.C., Andrews-Hanna, J.C., Asmar, S.W., 2013. The crust of the Moon as seen by GRAIL. Science 339, 671–675.

Wieczorek, M.A., Phillips, R.J., 1999. Lunar multiring basins and the cratering process. Icarus 139, 246–259.

Wieczorek, M.A., Phillips, R.J., 2000. The Procellarum KREEP Terrane: implications for mare volcanism and lunar evolution. J. Geophys. Res.-Planet. 105, 20417–20430.

Wieczorek, M.A., Simons, F.J., 2005. Localized spectral analysis on the sphere. Geophys. J. Int. 162, 655–675.

Wieczorek, M.A., Simons, F.J., 2007. Minimum-variance multitaper spectral estimation on the sphere. J. Fourier Anal. Appl. 13, 665–692.

Wöhler, C., Lena, R., Lazzarotti, P., Phillips, J., Wirths, M., Pujic, Z., Group, G.L.R.G.L.R., 2006. A combined spectrophotometric and morphometric study of the lunar mare dome fields near Cauchy, Arago, Hortensius, and Milichius. Icarus 183, 237–264.

Yamamoto, K., Haruyama, J., Ohtake, M., Iwata, T., Ishihara, Y., 2016. Relevance of the volcano complexes in the Western Oceanus Procellarum, Moon. In: Lunar and Planetary Science Conference, p. 1713.

Zhang, F., Zou, Y.L., Zheng, Y.C., Fu, X.H., Zhu, Y.C., 2014. Lunar mare basalts in the Aristarchus region: Implications for the stratigraphic sequence from Clementine UVVIS data. Icarus 227, 132–151.

Zuber, M.T., Smith, D.E., Neumann, G.A., Goossens, S., Andrews-Hanna, J.C., Head, J.W., Kiefer, W.S., Asmar, S.W., Konopliv, A.S., Lemoine, F.G., 2016. Gravity field of the Orientale basin from the gravity recovery and interior laboratory mission. Science 354, 438–441.